NANO · MICRO small
www.small-journal.com

Wafer-Scale Semitransparent MoS_2/WS_2 Heterojunction Catalyst on a Silicon Photocathode for Efficient Hydrogen Evolution

Jae Yoon Lee, Sang Eon Jun, Jae Hyung Shim, Hee Seong Kang, Changyeon Kim, Kitae Kim, Jin Yong An, Seokhoon Choi, Jeonghun Yun, Junghoon Kang, Seok Woo Lee, Soohyung Park, Hyunbok Lee, Yeonjin Yi, Ho Won Jang, and Chul-Ho Lee**

The development of catalysts that are optically transparent, electrically charge-transferable, and capable of protecting underlying photoactive semiconductors is crucial for efficient photoelectrochemical (PEC) hydrogen production. However, meeting all these requirements simultaneously poses significant challenges. In this study, the fabrication of a wafer-scale transparent bilayer MoS_2/WS_2 catalyst is presented with a staggered heterojunction, optimized for photon absorption, extraction of photogenerated charge carriers, and surface passivation of *p*-Si photocathode. The MoS_2 and WS_2 monolayers are grown via metal-organic chemical vapor deposition, followed by sequential transfer and stacking onto the *p*-Si photocathode. The resulting type-II heterojunction film establishes a strong built-in electric field for rapid charge carrier transport and effectively protects the Si surface from oxidation and corrosion. The fabricated MoS_2/WS_2/p-Si photocathode demonstrates outstanding PEC performance, achieving a high photocurrent density of −25 mA cm^{-2} at 0 V versus reversible hydrogen electrode, along with enhanced stability compared to monolayer MoS_2/p-Si. This work provides promising strategies for developing optically transparent, electrically active, and protective catalysts for practical PEC energy conversion systems.

1. Introduction

Photoelectrochemical (PEC) water splitting offers one of the cleanest ways to produce sustainable hydrogen energy production.[1,2] Among diverse semiconductor materials utilized in this process, including silicon,[3,4] gallium arsenide,[5] and copper (II) oxide,[6] earth-abundant *p*-type silicon (*p*-Si) has been widely utilized as a photocathode due to its optimal bandgap (1.12 eV), allowing for efficient absorption of a wide range of solar spectrum, and conduction band minimum positioned favorably above the hydrogen reduction potential (H^+/H_2).[7,8] Despite these advantages, silicon photocathodes face challenges such as insufficient output photovoltage, catalytic inactivity, and susceptibility to photo/chemical corrosion.[9] Consequently, there is a critical need for developing photoelectrochemical catalysts that can mitigate these issues by reducing potential

J. Y. Lee, J. H. Shim, H. S. Kang, J. Y. An
KU-KIST Graduate School of Converging Science and Technology
Korea University
Seoul 02841, Republic of Korea

J. Y. Lee, J. Yun, S. W. Lee
School of Electrical and Electronic Engineering
Nanyang Technological University
Singapore 639798, Singapore

S. E. Jun, C. Kim, S. Choi, H. W. Jang
Department of Materials Science and Engineering
Seoul National University
Seoul 08826, Republic of Korea
E-mail: hwjang@snu.ac.kr

The ORCID identification number(s) for the author(s) of this article can be found under https://doi.org/10.1002/smll.202407650

DOI: 10.1002/smll.202407650

S. E. Jun, C.-H. Lee
Inter-university Semiconductor Research Center
Seoul National University
Seoul 08826, Republic of Korea
E-mail: chulholee@snu.ac.kr

K. Kim, Y. Yi
Institute of Physics and Applied Physics
Yonsei University
Seoul 03722, Republic of Korea

K. Kim, Y. Yi
Van der Waals Materials Research Center
Yonsei University
Seoul 03722, Republic of Korea

K. Kim, S. Park
Advanced Analysis Center
Korea Institute of Science and Technology (KIST)
Seoul 02792, Republic of Korea

J. Kang, C.-H. Lee
Department of Electrical and Computer Engineering
Seoul National University
Seoul 08826, Republic of Korea

barriers, enhancing catalytic activity, and passivating the surface of *p*-Si for efficient solar-assisted hydrogen production.[10]

Recently, 2D transition metal dichalcogenides (TMDs) like MoS_2, $MoSe_2$, WS_2, and NbS_2 have garnered attention for improving the PEC performance of silicon photocathodes due to their cost-effectiveness and optimal hydrogen adsorption Gibbs free energy (ΔG_H).[11–14] In particular, atomic defects (vacancies and grain boundaries),[15–17] dopants,[18] and metallic edges in TMDs have exhibited notable catalytic activity in the hydrogen evolution reaction (HER).[19,20] Various synthetic methods based on chemical vapor reactions, including powder source chemical vapor deposition (CVD),[21] sulfurization of pre-deposited transition metal films (Mo or W),[22] and thermolysis of liquid-phase precursors,[12] have been employed to synthesize wafer-scale thin-film TMDs on silicon photocathodes. Although these methods enable scalable synthesis of TMDs, achieving high spatial uniformity and layer control over a wafer-scale substrate remains challenging. Given that three-atom-thick semiconducting TMDs effectively prevent parasitic light absorption and reduce photoinduced charge recombination,[23] advancing the fabrication techniques for silicon photocathodes incorporating monolayer TMDs with superior spatial homogeneity is imperative. Moreover, precise transfer and stacking processes are crucial, as direct growth of TMDs on silicon photocathodes often leads to chemical incompatibility, formation of secondary compounds, and interfacial defects, ultimately resulting in poor stability and the occurrence of leakage current.[24]

Metal-organic chemical vapor deposition (MOCVD) has emerged as a powerful technique utilizing finely controllable vapor-phase precursors to produce highly uniform and layer-controlled TMD films over a wafer scale.[25,26] Additionally, MOCVD-grown monolayer TMD films can be easily transferred onto arbitrary substrates without encountering chemical incompatibility or interfacial defects. The wafer-scale assembly of multi-layer TMD heterostructures with atomic precision control and clean interface has been reported for electronic device applications.[27] Taking advantages of the MOCVD technique and the produced films, it is feasible to integrate silicon photocathodes with large-scale, highly uniform, and atomically thin bilayer TMD heterostructures, optimized for photon harvesting, extraction of photogenerated charge carriers, and surface passivation.

Here, we present the first demonstration of a wafer-scale semi-transparent bilayer MoS_2/WS_2 catalyst with a staggered heterojunction to enhance the PEC hydrogen evolution of *p*-Si photocathodes. The highly uniform MoS_2 and WS_2 monolayers are successfully grown by a home-built MOCVD system, with the properties comparable to those of exfoliated single-crystal counterparts. The atomically thin TMD layers synthesized via precisely controlled MOCVD exhibit high light transmittance, enabling significant absorption of incident light by the photocathode. Furthermore, the type-II heterojunction of MoS_2 and WS_2 creates a strong built-in electric field that facilitates charge carrier transport at the semiconductor/electrolyte interface. Moreover, the bilayer MoS_2/WS_2 outperforms monolayer MoS_2 in protecting the Si surface. Consequently, the silicon photocathode with the bilayer MoS_2/WS_2 catalyst demonstrates outstanding PEC hydrogen evolution performance, with a low onset potential of 0.17 V versus RHE and a high photocurrent density of -25 mA cm^{-2} at 0 V versus RHE. Our novel approach to synthesizing high-quality monolayer TMDs using MOCVD and constructing bilayer TMDs with type-II heterojunction offers substantial benefits for PEC water splitting in terms of scalability, photon absorption, interfacial charge transport, and stability.

2. Results and Discussion

Figure 1a shows a schematic of PEC hydrogen production using a wafer-scale *p*-Si photocathode uniformly coated with MoS_2/WS_2 heterojunction films. The atomically thin MoS_2/WS_2 heterojunction catalyst facilitates PEC-HER [$2H^+ + 2e^- \rightarrow H_2$] by lowering the energy barrier ($\Delta G_1 \rightarrow \Delta G_2$) of electrochemical reaction.[28] Furthermore, as illustrated in Figure 1b, a staggered type-II band alignment can be established through the stacking of monolayer WS_2 and MoS_2 on *p*-Si.[29] This cascade band alignment induces a strong built-in electric field and substantial band bending underneath the Si interface, which accelerate the separation and transport of photoexcited electrons from the light-absorbing semiconductor to semiconductor/electrolyte interface.[30] Moreover, the moderate passivation of the silicon surface employing atomically thin film catalyst prevents the chemical oxidation and photoinduced corrosion of silicon photoabsorber.

The wafer-scale monolayer TMDs, including MoS_2 and WS_2, are grown using MOCVD with molybdenum hexacarbonyl (MHC, 99.9%), tungsten hexacarbonyl (THC, 99.99%), and diethyl sulfide (DES, 98%) as Mo, W, and S precursors, respectively (see the detailed synthesis method in the experimental section). Our MOCVD system, featuring a vertical, cold-wall chamber equipped with a radio frequency induction heater and rotation sample holder facilitates uniform thin film growth while minimizing side reactions. Moreover, precise control over the molar flow rate of each precursor allows us to achieve the growth of homogeneous monolayer TMD films on a 2-inch SiO_2/Si substrate.

Figure 1c illustrates the experimental procedure and presents the photographic images depicting the sequential transfer of individual TMD monolayers onto the *p*-Si. Specifically, poly[methyl methacrylate] (PMMA) is spin-coated onto each TMD film, and thermal release tapes (TRT) are subsequently attached to the PMMA/TMD films. The TRT/PMMA/WS_2 film is then peeled off and transferred onto the *p*-Si substrate treated with hydrogen fluoride (HF) to remove a native oxide. Subsequently, the TRT and PMMA layers are removed by heating and dipping into the acetone, respectively, resulting in a WS_2/p-Si photocathode. Following the same procedure, the MoS_2 layer is transferred onto the WS_2/p-Si, yielding a van der Waals

H. Lee
Department of Physics
Kangwon National University
Chuncheon 24341, Republic of Korea
H. Lee
Institute for Accelerator Science
Kangwon National University
Chuncheon 24341, Republic of Korea
H. W. Jang
Advanced Institute of Convergence Technology
Seoul National University
Suwon 16229, Republic of Korea

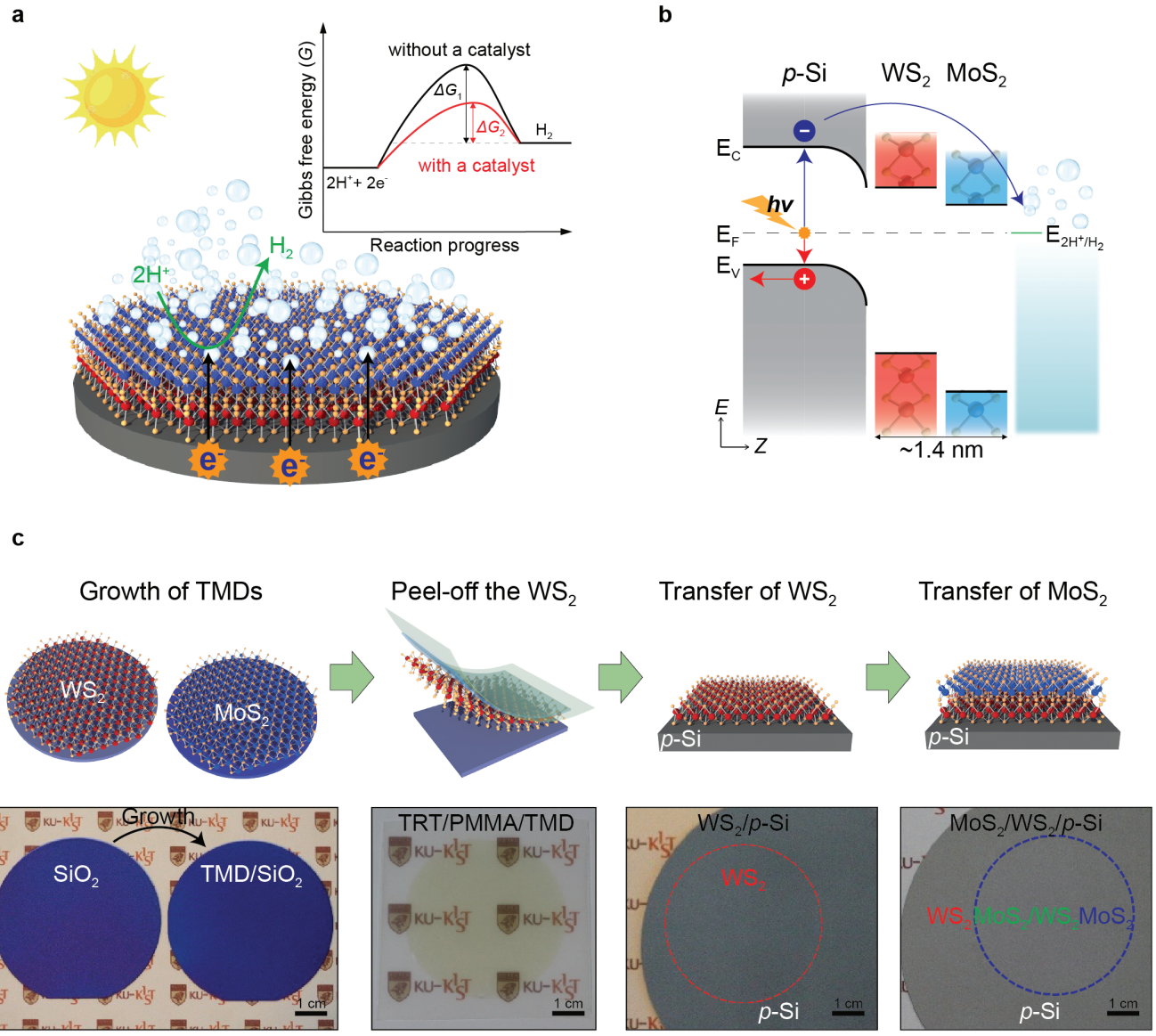

Figure 1. Wafer-scale heterojunction film catalyst made of stacked MoS_2/WS_2 hetero-bilayers on a *p*-type Silicon photocathode for efficient HER. a) Schematic and b) band diagram of a *p*-Si photocathode with the atomically thin MoS_2/WS_2 heterojunction film as a catalyst. The graph in (a) is general changes in Gibbs free energy according to the reaction progress without (black solid line, ΔG_1) or with (red solid line, ΔG_2) the monolayer MoS_2/WS_2 heterojunction catalyst. The staggered type-II band alignment can promote the separation and transport of photoexcited electrons from the *p*-Si to the electrolyte. c) Schematic (top) of sequential transfer and fabrication procedure of the monolayer MoS_2/WS_2 heterojunction film catalyst on a *p*-Si photocathode. The corresponding photographic images (bottom) of each step. Before and after MOCVD growth of monolayer TMDs (MoS_2 and WS_2) onto the 2-inch SiO_2/Si substrate (step 1). The 2-inch WS_2 film by mechanically peeled off using the thermal release tape (step 2). The transferred WS_2 onto the *p*-Si and the sequentially stacked MoS_2 on the WS_2/p-Si (step 3, 4). Scale bars are 1 cm.

(*vdW*)-stacked $MoS_2/WS_2/p$-Si photocathode. Photographic images demonstrate the high transparency of TMDs, indicating anticipated high photon absorption of the *p*-Si photocathode. Finally, back contact and device passivation processes are carried out for PEC measurements (see the details of the fabrication procedure in Figure S1, Supporting Information).

Figure 2a shows 3D surface morphology images and line profiles of each film obtained by atomic force microscopy (AFM) measurements. The film thicknesses are determined to be 0.7 nm for the monolayer MoS_2 (and WS_2) and 1.5 nm for the hetero-bilayer MoS_2/WS_2, consistent with previously reported values for monolayer TMDs and vertically stacked heterostructure.[31] The surface roughness (root mean square, RMS) of MoS_2, WS_2, MoS_2/WS_2, and WS_2/MoS_2 is measured at 0.244, 0.321, 0.322, and 0.327 nm, respectively (Figure S2, Supporting Information), indicating atomically flat and pristine surfaces of transferred films and high-quality heterojunction formation regardless of stacking order.

The transmittance spectra of monolayer MoS_2, WS_2, and the hetero-bilayer MoS_2/WS_2 films are measured by ultraviolet

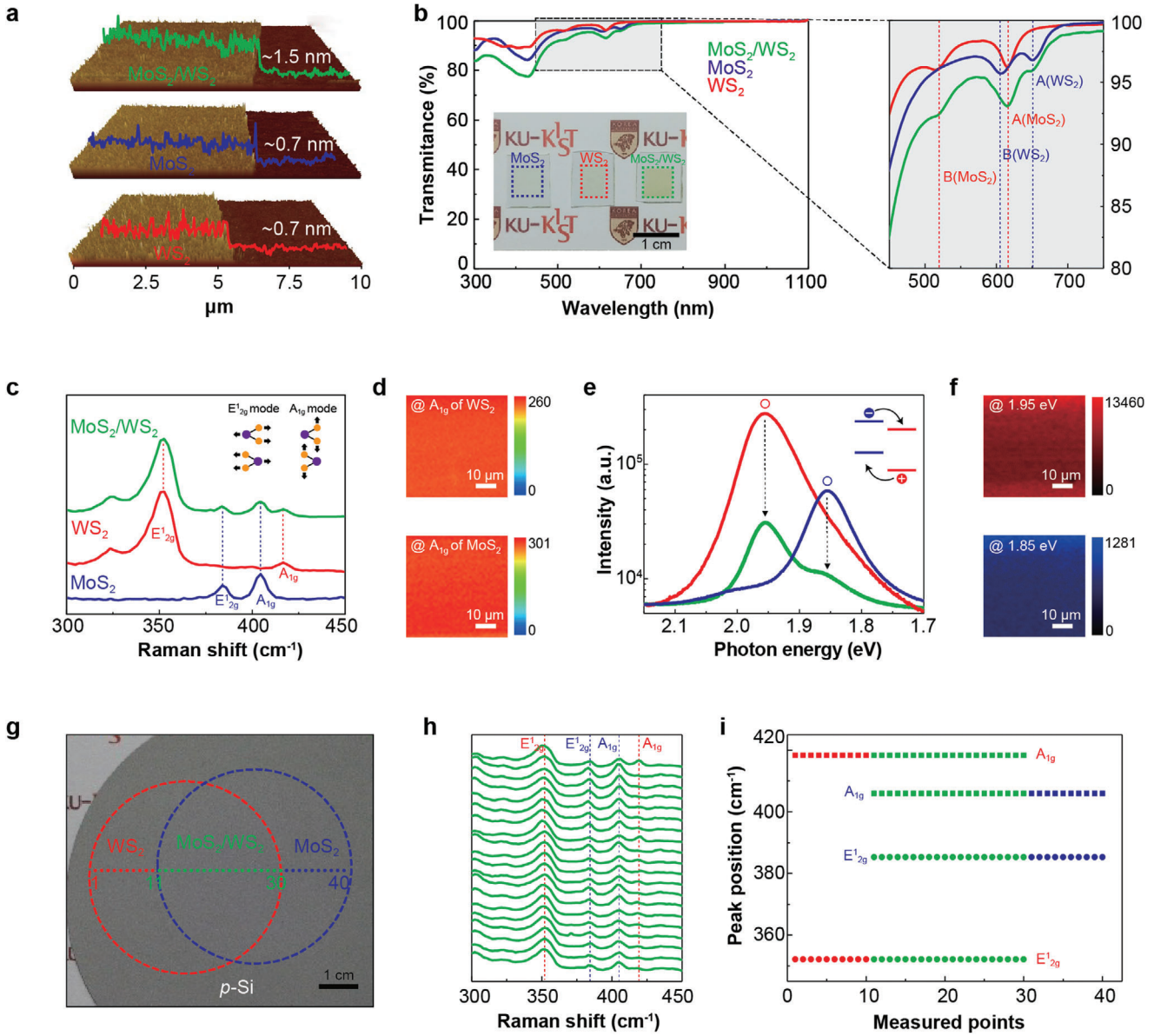

Figure 2. Optical characterization of the hetero-bilayer MoS_2/WS_2, monolayer MoS_2, and monolayer WS_2 films. a) Atomic force microscopy (AFM) 3D topography images and average line profiles of the monolayer MoS_2/WS_2 heterostructure (top), monolayer MoS_2 (middle), and monolayer WS_2 (bottom) films on the 285-nm SiO_2/Si substrates, respectively. b) Transmittance spectra of the monolayer MoS_2/WS_2 heterostructure (green solid line), monolayer MoS_2 (blue solid line), and monolayer WS_2 (red solid line) films on quartz substrates, respectively. Inset: the photographic image of the transferred films on the sapphire substrates, respectively. The scale bar is 1 cm. The right graph is the magnified graph of the dashed box. c) Raman spectra of each structure on the 285-nm SiO_2/Si substrates. d) Raman mapping images of the MoS_2/WS_2 hetero-bilayers at each A_{1g} mode, respectively. e) PL spectra of each structure on the 285-nm SiO_2/Si substrates. f) PL mapping images of MoS_2/WS_2 hetero-bilayers at 1.95 eV for WS_2 and 1.85 eV for MoS_2, respectively. g) Photographic image of the 2-inch transferred MoS_2/WS_2 hetero-bilayers on the 4-inch *p*-Si wafer with indicated laser spots for Raman spectra of 40 points. The scale bar is 1 cm. h) Raman spectra of the transferred MoS_2/WS_2 (green) on *p*-Si substrate for a total of 20 points. i) Line profiles of peak positions for WS_2 (red), MoS_2 (blue), and MoS_2/WS_2 hetero-bilayers (green).

(UV)-visible spectroscopy after transferring the films onto *c*-plane sapphire (*c*-sapphire) substrates, as shown in the inset image of Figure 2b. In the magnified graph of Figure 2b and Figure S3 (Supporting Information), the A and B exciton peaks of each TMD film are directly observed at 650 and 605 nm for MoS_2, and 616 and 515 nm for WS_2, respectively. The preservation of exciton peaks after the transfer and stacking processes indicate the formation of high-quality heterointerfaces and the robustness of these processes. Moreover, the MoS_2/WS_2 heterojunction demonstrates remarkably high light transmittance of ≈92.5%, extending beyond the 600 nm wavelength range. This high transmittance is advantageous for efficient photon absorption by the *p*-Si photocathode, consequently leading to a high photocurrent density.

Thin film catalysts are further characterized using Raman spectroscopy, X-ray photoelectron spectroscopy (XPS), and low-angle grazing incidence X-ray diffraction (GIXRD). Figure 2c presents the Raman spectra of monolayer MoS_2, WS_2, and hetero-bilayer MoS_2/WS_2. The main vibration modes for TMD structures, including the $E^1_{2\,g}$ (in-plane mode) and $A_{1\,g}$ (out-of-plane mode), are observed at 383.04 ($E^1_{2\,g}$) and 401.64 ($A_{1\,g}$) cm^{-1} for monolayer MoS_2 (blue line), and 351.92 ($E^1_{2\,g}$), and 417.14 ($A_{1\,g}$) cm^{-1} for monolayer WS_2 (red line).[32,33] Additionally, the identical Raman peaks (green line) without a noticeable shift are observed in the vertically stacked MoS_2/WS_2, confirming the high-quality heterojunction formation without substantial compositional mixing and electronic hybridization. XPS measurements are also conducted to analyze the chemical binding state of MoS_2, WS_2, and their heterojunction on *p*-Si (Figure S5, Supporting Information). The deconvoluted XPS spectra of the Mo 3*d*, W 4*f*, and S 2*p* elements clearly indicate the presence of the 2H phase in both MoS_2 and WS_2. No peak shift in the binding energy is observed between individual monolayers and their hetero-bilayer, implying that no chemical reaction or interaction occurs between MoS_2 and WS_2 during the stacking process.[34,35] Furthermore, low-angle GIXRD pattern of the MoS_2/WS_2 heterostructure exhibits a distinct peak at 14.5° (Figure S6, Supporting Information), corresponding to the *vdW* gap. This peak is absent in the patterns of monolayer MoS_2 and WS_2.

Meanwhile, as shown in Figure 2e, the PL spectra of MoS_2 (1.85 eV, blue line) and WS_2 (2.00 eV, red line) clearly indicate the direct bandgap transition corresponding to the monolayer TMD characteristics of each layer. The PL intensity of the MoS_2/WS_2 heterostructure is sharply quenched. It indicates that ultrafast charge transfer spontaneously occurs due to the cascade type-II band alignment, which is also consistent with our previous report.[31]

Given the critical importance of uniformity and scalability in thin film TMD catalysts for practical applications, the spatial-resolved Raman and PL intensity mapping images are acquired across 25 μm × 50 μm area to verify the high quality of the MOCVD-grown monolayer MoS_2 and WS_2 (Figure 2d,f). Both MoS_2 and WS_2 exhibit high optical uniformity in the Raman and PL mapping based on $A_{1\,g}$ atomic vibration peak and each exciton peak, respectively. Additionally, Raman spectra are obtained at multiple points from three spatially distinct regions of MoS_2, WS_2, and MoS_2/WS_2 on the transferred films on a *p*-Si wafer (Figure 2g,h; Figure S4, Supporting Information). In Figure 2i, the line profiles of peak positions for WS_2, MoS_2, and MoS_2/WS_2 hetero-bilayers exhibit a uniform distribution of each characteristic peak. These results confirm that the wafer-scale monolayer TMD films grown by MOCVD exhibit remarkable uniformity and scalability even after integration on the *p*-Si photocathode, rendering them suitable for large-scale hydrogen production.

The photoelectrochemical HER performance of the prepared photocathodes with TMD catalysts is measured under simulated air mass 1.5 G solar illumination with a standard three-electrode system in a 0.5 M H_2SO_4 electrolyte. **Figure 3a** presents the PEC photocurrent density of bare p-Si, MoS_2/*p*-Si, WS_2/p-Si, and MoS_2/WS_2/*p*-Si photocathodes as a function of the applied potential with respect to the reversible hydrogen electrode (RHE). The bare *p*-Si photocathode without a catalyst exhibits a highly negative onset potential of −0.54 V versus RHE to achieve a photocurrent density of −1 mA cm^{-2} due to its catalytic inactivity for HER. The onset potential largely shifts toward the anodic direction by introducing both monolayer MoS_2 and WS_2 catalysts on the *p*-Si photocathode, which is attributed to their high catalytic activity and the built-in electric field between *p*-Si and *n*-type TMDs. Notably, dramatically enhanced PEC-HER performance is accomplished by applying a MoS_2/WS_2 heterojunction catalyst to *p*-Si, with an onset potential of 0.17 V versus RHE and a photocurrent density of −25 mA cm^{-2} at 0 V versus RHE. Interestingly, there is a negligible difference in saturation current density between bare *p*-Si and that coated with MoS_2/WS_2 catalyst. It indicates that atomically thin heterostructure TMDs exhibit excellent light transmittance and facilitate photogenerated electron transfer. The enhancement of the PEC performance can be further confirmed by electrochemical impedance spectroscopy (EIS) by measuring the charge-transfer resistance at the interfaces. Figure 3b presents the Nyquist plots of photocathodes measured by applying −0.16 V versus RHE and these plots are fitted to a simplified equivalent circuit consisting of two constant phase elements (CPE_1, CPE_2) and two charge transfer resistances (R_1, R_2). All samples show single semicircles in the Nyquist plots despite multiple interfaces, implying negligible interfacial resistance between *p*-Si and TMDs due to the formation of favorable *p*-*n* junction and high-quality heterointerfaces achieved by vertical *vdW* integration. The charge transfer resistance (R_2) value for the MoS_2/WS_2/*p*-Si (148.42 Ω cm^2) is considerably lower than those for monolayer MoS_2 (990.41 Ω cm^2) and WS_2 (755.48 Ω cm^2). In spite of the identical top surfaces of both MoS_2/*p*-Si and MoS_2/WS_2/*p*-Si, MoS_2/WS_2/*p*-Si shows much lower interfacial resistance. It indicates that cascade band alignment leads to favorable energy band bending, which accelerates the photo-induced electron transfer at the TMDs/electrolyte interface.

In Figure 3c, the incident-photon-to-current conversion efficiency (IPCE) is measured to analyze the performance of photocathodes converting the incident light to electrical current density. It is measured from 300 to 800 nm of wavelength at applied potential of 0 V versus RHE. For the photocathodes with single TMDs, the efficiency is ≈30% on average from the wavelength of 400 nm. By introducing a MoS_2/WS_2 heterojunction catalyst, the efficiency is remarkably increased over the entire visible light wavelength and it reaches up to 80%.

To investigate the passivation capability of bilayer MoS_2/WS_2 heterojunction catalyst, cyclic voltammetry tests are carried out. Figure 3d shows polarization curves of bare *p*-Si (black), MoS_2/*p*-Si (blue), and MoS_2/WS_2/*p*-Si (green) photocathodes during 100 cycles (all curves are shown in Figure S7, Supporting Information). After cyclic test, polarization curve of bare *p*-Si photocathode shifts negatively due to surface degradation derived from the formation of insulating SiO_2. Similarly, the PEC performance of MoS_2/*p*-Si photocathode dramatically decreased after cyclic test, implying that the monolayer MoS_2 does not fully protect the Si surface and suppress the degradation. However, in the case of MoS_2/WS_2/*p*-Si photocathode, its initial performance is completely maintained without negative shift of polarization curve. In Figure 3e, the numerical potentials of photocathodes to achieve a photocurrent density of −10 mA cm^{-2} are plotted according to the scan number. From these results, it is confirmed that

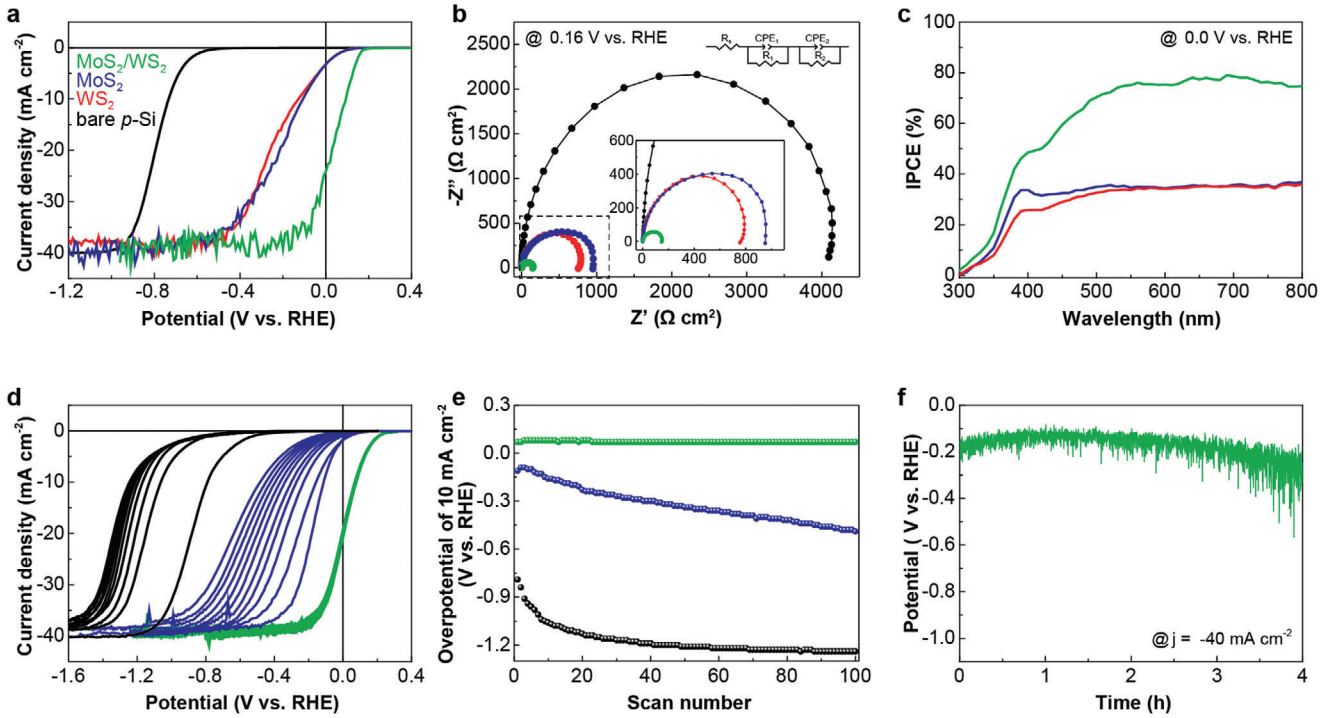

Figure 3. Photoelectrochemical (PEC) characterization of *p*-Si photocathodes with different TMD-based catalysts under global illumination. a) Polarization curves of *p*-Si photocathodes with the MoS_2/WS_2 (green solid line), MoS_2 (blue solid line), WS_2 (red solid line), and no catalyst (bare *p*-Si, black solid line). b) Nyquist impedance plots of each photocathode under illumination at 0.16 V versus RHE from 350 kHz to 0.1 Hz. The inset is the magnified graph of the dashed box. c) IPCE spectra of each photocathode at 0.0 V versus RHE from 300 to 800 nm. d) Polarization curves of the 1st, 10th, 20th, 30th, 40th, 50th, 60th, 70th, 80th, 90th, and 100th cycles of the MoS_2/WS_2, MoS_2, no catalyst on the *p*-Si photocathode to compare their stabilities. e) Comparison of the overpotentials to achieve a photocurrent density of 10 mA cm^{-2} converted from the panel (d). f) Chronopotentiometry measurements of the MoS_2/WS_2/*p*-Si photocathode.

hetero-bilayer TMDs provide much better passivation of the Si surface compared to monolayer TMDs. Furthermore, the long-term stability of MoS_2/WS_2/*p*-Si photocathode is investigated by chronopotentiometry measurement to achieve a photocurrent density of −40 mA cm^{-2} in Figure 3f. The photoelectrochemical degradation of silicon photocathode is considerably suppressed with maintaining its initial performance over 4 h. After the long-term stability test, no noticeable peak shifts or intensity degradation are observed in the Raman spectrum, indicating the absence of significant defect generation, disorder, dissolution, and phase transitions (Figure S8, Supporting Information). The Faradaic efficiency of the MoS_2/WS_2/*p*-Si is determined by collecting the evolved hydrogen gas during the PEC reaction and almost 100% Faradaic yield is obtained (Figure S9, Supporting Information).

To further highlight the effect of TMD stacking order on PEC performance, a WS_2/MoS_2/*p*-Si photocathode with a reverse stacking order was prepared for comparison. As shown in **Figure 4**a,b, and Table S1 (Supporting Information), the reverse-ordered WS_2/MoS_2/*p*-Si exhibits a more negative overpotential of 0.16 V and a lower saturation current density of 34.96 mA cm^{-2} compared to the MoS_2/WS_2/*p*-Si. Furthermore, it shows a higher interfacial resistance, as illustrated in Figure 4c, indicating that charge transport is suppressed due to the reverse stacking order. Its PEC performance is even inferior to that of photocathodes with monolayer MoS_2 or WS_2 (Figure S10, Supporting Information). These results may be attributed to the recombination of photogenerated charge carriers caused by reverse ordered band alignment of WS_2/MoS_2/*p*-Si.[23,31,36–39]

To elucidate the electron transport mechanism depending on the stacking order of TMDs, the electronic band alignments of MoS_2/WS_2/*p*-Si and WS_2/MoS_2/*p*-Si are illustrated using UPS analysis. For MoS_2/WS_2/*p*-Si, as shown in Figure 4e, the measured work functions of *p*-Si, WS_2/*p*-Si, and MoS_2/WS_2/*p*-Si are 4.59, 3.72, and 3.71 eV, respectively, consistent with previous reports based on DFT calculations.[40,41] The energy differences between the Fermi level and the valence band maximum (E_F-E_V) are 0.33, 2.03, and 1.94 eV. Based on these results and the measured electrical bandgaps (2.18 eV for MoS_2, 2.40 eV for WS_2) obtained from scanning tunneling microscopy (STM), the schematic of the energy band diagram is depicted in Figure 4d. The MoS_2/WS_2/*p*-Si configuration shows a staggered band alignment, which efficiently transfers photogenerated electrons to the electrolyte. The conduction band minimum (CBM) difference between WS_2 and MoS_2 creates a strong built-in electric field, facilitating rapid charge transfer without recombination.[42,43] In contrast, the band structure of reversely stacked WS_2/MoS_2/*p*-Si (Figure 4f) exhibits a large energy barrier between MoS_2 and WS_2, disrupting electron transfer from the MoS_2 layer to the WS_2 and leading to charge recombination. These findings clearly demonstrate that optimizing band alignment through precise stacking significantly improves the photoelectrochemical performance of the silicon photocathode.

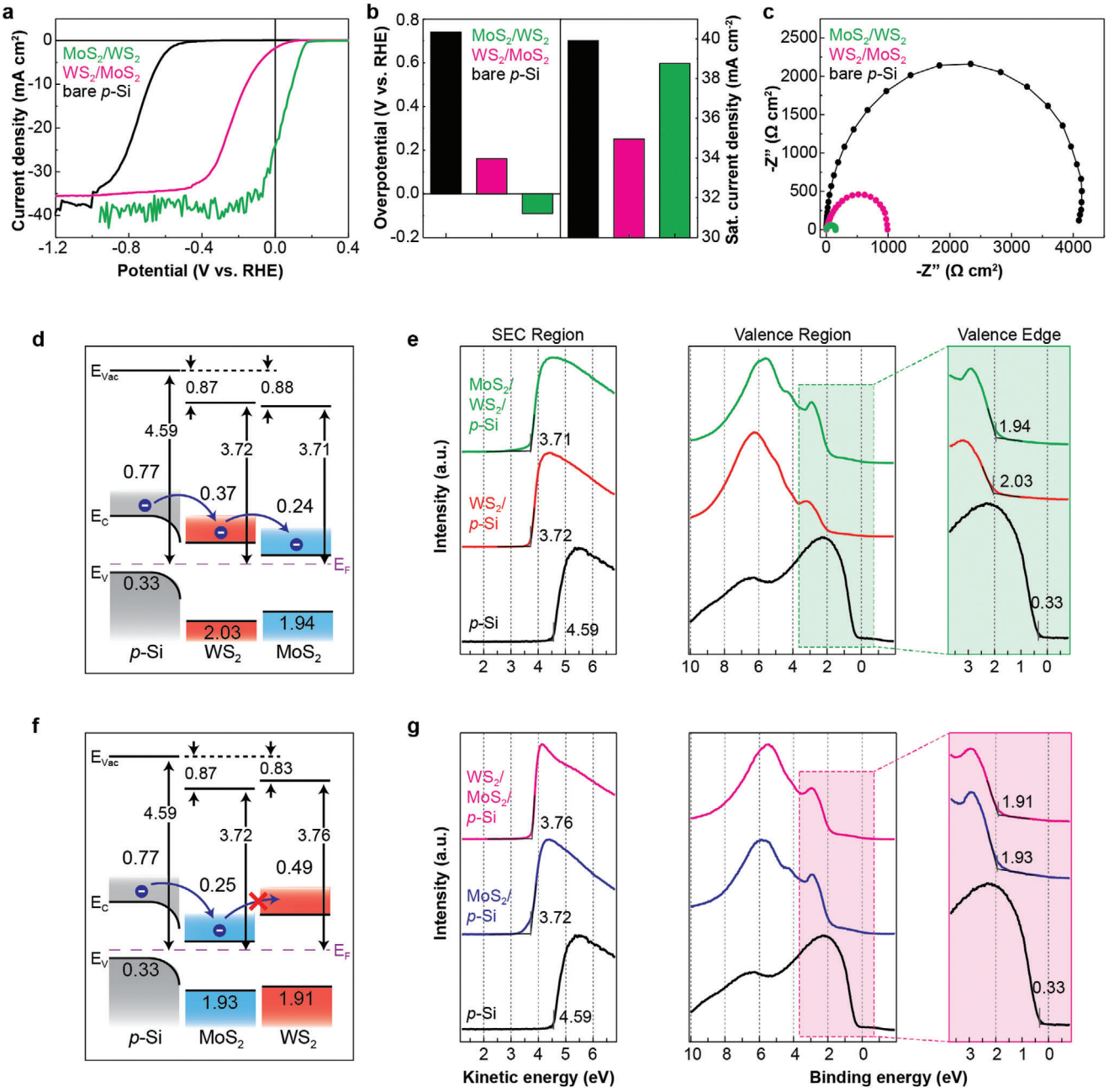

Figure 4. PEC characterization and band diagram of *p*-Si photocathodes with the MoS_2/WS_2 and reverse ordered WS_2/MoS_2 heterojunction catalysts. a) Polarization curves of *p*-Si photocathodes with the MoS_2/WS_2 (green solid line), reverse ordered WS_2/MoS_2 (magenta solid line), and no catalyst (bare *p*-Si, black solid line). b) Nyquist impedance plots of each photocathode. c) Comparison of the overpotentials at 10 mA cm^{-2} (left) and the saturated (Sat.) current densities (right) of each photocathode. d,f) Energy band diagrams of the MoS_2/WS_2/*p*-Si and WS_2/MoS_2/*p*-Si heterojunctions. e,g) Ultraviolet photoemission spectroscopy (UPS) spectra of the MoS_2/WS_2/*p*-Si (green solid line), WS_2/*p*-Si (red solid line), reverse ordered WS_2/MoS_2/*p*-Si (magenta solid line), MoS_2/*p*-Si (blue solid line), bare *p*-Si (black solid line), respectively.

3. Conclusion

In summary, we successfully demonstrate wafer-scale transparent and charge-transferable MoS_2/WS_2 heterojunction film catalyst for highly efficient PEC-HER. The atomically thin type-II heterojunction catalyst not only provides a substantial built-in electric field for facile photogenerated charge transport at the semiconductor/electrolyte interface, but also serves as a passivation layer preventing surface degradation of a photoelectrode. Consequently, silicon photocathode with the MoS_2/WS_2 heterojunction catalyst exhibits an outstanding PEC hydrogen evolution performance with the photocurrent density of −25 mA cm^{-2} at 0 V versus RHE. This study suggests an effective strategy for integrating large-scale and ultrathin heterojunction catalysts on

semiconducting photocathodes and broadens our fundamental understanding of band structure engineering for photoelectrochemical water splitting.

4. Experimental Section

Synthesis of Monolayer MoS_2 and WS_2 Films: Monolayer MoS_2 and WS_2 films were grown using home-built metal-organic chemical vapor deposition. For metal-organic Mo, W, S precursors, the molybdenum hexacarbonyl (MHC, 99. 9%), tungsten hexacarbonyl (THC, 99.99%), and diethyl sulfide (DES, 98%), were used respectively. Before the growth, 0.25 M NaCl solution as growth promoter was spin-coated at 2000 rpm for 15 s and baked for 1 min at 180 °C on a 2-inch SiO_2/Si substrate. Next, the NaCl solution treated substrate was placed into graphite susceptor in a vertical MOCVD reactor, heated to growth temperature (600 °C). During the growth process, 5.41×10^{-13} mole min^{-1} for MHC (8.35×10^{-14} mole min^{-1} for THC) and 6.59×10^{-11} mole min^{-1} for DES were introduced into a vertical reactor. The growth was performed for 240 min at 50 Torr, and MoS_2 and WS_2 films were naturally cooled down to room temperature.

Transfer Process and Device Fabrication: To fabricate the atomically thin heterojunction ($MoS_2/WS_2/p$-Si), MOCVD-grown TMDs (MoS_2 and WS_2) films were transferred onto the *p*-Si substrate using the drying mechanical peeling method, which was known as the vdW layer-by-layer assembly. First, poly(methylmethacrylate) (PMMA, A4 495K, MicroChem.) was spin-coated onto the as-grown 1st WS_2/SiO_2/Si substrates at 4000 rpm for 90 s and baked at 180 °C for 10 min. And then, the thermal release tape (TRT, Graphene Square) was attached onto the PMMA/WS_2 film, and TRT/PMMA/WS_2 film was mechanically peeled from the SiO_2/Si substrate. Prior to the TMD transfer, the *p*-Si substrates were treated by HF solution to remove the native oxide on the *p*-Si surface. After the separated TRT/PMMA/WS_2 film was transferred onto the HF treated *p*-Si substrate, the TRT was released from the substrate by heating at 110 °C for 2 min. Then, post-annealing for the PMMA/WS_2/p-Si was performed at 180 °C for 10 min to improve the adhesion between the WS_2 layer and *p*-Si. To remove the PMMA, the sample was dipped in acetone for 20 min and cleaned to rinse the remaining acetone on the surface using the IPA. To make the MoS_2/WS_2/p-Si heterostructure, the same abovementioned process was repeated about the as-grown 2nd MoS_2 film on the SiO_2/Si substrate.

To fabricate the PEC device, the backside of the $MoS_2/WS_2/p$-Si sample was scratched and blown by the high purity N_2 gas. Subsequently, the In-Ga eutectic alloy was coated onto the back of the sample, and copper wire was attached using the silver paste. After drying the sample for 1 h, the mixture of the epoxy and resin for a 1:1 ratio was used to passivate the final device structure except for the activation window region sized with 0.5×0.5 cm^2. Figure S1 (Supporting Information) illustrates the whole process for transfer and making the final PEC device.

Materials Characterization: The transmittance and absorbance spectra of monolayer MoS_2, WS_2, and the monolayer MoS_2/WS_2 heterostructure films, which were transferred onto transparent c-sapphire by dry-transfer process, were obtained by using the UV-visible spectrometer (Agilent, 8453E) with a spectral range from 190 to 1100 nm. To estimate the thickness and surface morphology of these films, atomic force microscopy (AFM, Park systems, XE-10) was used. Optical characterization including Raman and Photoluminescence (PL) spectra were evaluated by using a home-built spectrometer combined with a monochromator (Andor, SOLIS 303i) and an excitation laser of 532 nm under ambient conditions. The PL and Raman signals were collected by an objective lens (NIKON 100×, N.A. = 0.9), and dispersed by 1200 and 300 line mm^{-1} gratings for Raman and PL measurements, respectively. The spatially resolved PL and Raman mapping was performed to confirm the optical uniformity by using the X-Y scanning the films on the motorized stage in the optical spectrometer system. The work function, valance band maximum, and band alignment of TMD heterostructures were estimated by ultraviolet photoelectron spectroscopy (UPS, ULVAC-PHI). The UPS measurement were carried out using the He I (21.22 eV) beam as an ultraviolet light source, and the binding energy reference was calibrated by the Fermi-edge of a clean Au film. X-ray photoelectron spectroscopy (XPS) measurements was performed using an X-tool (ULVAC-PHI) with Al K_α X-ray source (1486.6 eV, 24.1 W, and 15 kV) under the ultrahigh vacuum chamber with the base pressure of $\approx 10^{-10}$ Torr.

PEC Measurements: All PEC measurements were performed by an Ivium potentiostat (Ivium Technologies, Compact-stat) with a three-electrode system using a Pt mesh counter electrode, a saturated calomel reference electrode, and a working electrode in a 0.5 M H_2SO_4 standard electrolyte solution. The three-electrode and the electrolyte solution were built inside a quartz bath. The conversion equation of potential versus RHE is expressed as the following equation:

$$E_{RHE} = E_{SCE} + E^{\circ}{}_{SCE} + 0.059 \times \mathrm{pH} \ (E^{\circ}{}_{SCE} = 0.242 \ vs.\ RHE) \quad (1)$$

where the E_{SCE} is the potential of the saturated calomel electrode, the $E^{\circ}{}_{SCE}$ is the potential of the saturated calomel electrode concerning the standard hydrogen potential (SHE), and the pH in 0.5 M H_2SO_4 electrolyte is 0.27. A Xe arc lamp calibrated to an output power of 100 mW cm^{-2} (corresponding to the air mass 1.5 global (AM 1.5 G) condition) was used as a global illumination source. A scan rate of 10 mV s^{-1} was used for the linear sweep. Electrochemical impedance spectroscopy (EIS) was conducted by applying a constant potential of 0.16 V versus RHE with a sweeping frequency from 350 kHz to 0.1 Hz. Incident-photon-to-current conversion efficiency (IPCE) was conducted by applying a constant potential of 0.0 V versus RHE with the same lamp and monochromator. The efficiency was calculated by the following equation:

$$IPCE\ (\lambda) = EQE\ (\lambda) = \frac{\left| j_{ph}\ (mA/cm^2) \right| \times 1239.8\ (V \times nm)}{P_{mono}\ (mW/cm^2) \times \lambda\ (nm)} \quad (2)$$

where the j_{ph} is photocurrent of the photoelectrode, the λ is the wavelength, and the P_{mono} is the power of the monochromator. The external quantum efficiency was calibrated by a Si photodiode. Faradaic efficiency was conducted with a gas chromatography measurement system (FID-GC, PerkinElmer, NARL8502 Model 4003).

Supporting Information

Supporting Information is available from the Wiley Online Library or from the author.

Acknowledgements

J.Y.L., S.E.J., and J.H.S. contributed equally to this work. This research was supported by the National Research Foundation (NRF) of Korea grant, funded by the Korean government (MSIT) (2023R1A2C3005923, 2022M3H4A1A01010280, and 2021M3H4A1A03057403). C.-H.L acknowledges the support from BK21 FOUR program of the Education and Research Program for Future ICT Pioneers, Creative-Pioneering Researchers Program through Seoul National University, the Inter-University Semiconductor Research Center (ISRC), and the Institute of Applied Physics (IAP) at the Seoul National University.

Conflict of Interest

The authors declare no conflict of interest.

Data Availability Statement

The data that support the findings of this study are available from the corresponding author upon reasonable request.

Keywords

catalysts, metal-organic chemical vapor deposition, photoelectrochemical water splitting, silicon, transition metal dichalcogenides

Received: August 28, 2024
Revised: October 13, 2024
Published online: October 31, 2024

[1] J. F. Gibbons, G. W. Cogan, C. M. Gronet, N. S. Lewis, *Appl. Phys. Lett.* **1984**, *45*, 1095.
[2] M. G. Walter, E. L. Warren, J. R. McKone, S. W. Boettcher, Q. Mi, E. A. Santori, N. S. Lewis, *Chem. Rev.* **2010**, *110*, 6446.
[3] S. E. Jun, Y.-H. Kim, J. Kim, W. S. Cheon, S. Choi, J. Yang, H. Park, H. Lee, S. H. Park, K. C. Kwon, J. Moon, S.-H. Kim, H. W. Jang, *Nat. Commun.* **2023**, *14*, 609.
[4] S. Choi, S. A. Lee, J. W. Yang, W. Sohn, J. Kim, W. S. Cheon, J. Park, J. H. Cho, C. W. Lee, S. E. Jun, S. H. Park, J. Moon, S. Y. Kim, H. W. Jang, *J. Mater. Chem. A* **2023**, *11*, 17503.
[5] O. Khaselev, J. A. Turner, *Science* **1998**, *280*, 425.
[6] A. Paracchino, V. Laporte, K. Sivula, M. Grätzel, E. Thimsen, *Nat. Mater.* **2011**, *10*, 456.
[7] D. M. Andoshe, S. Choi, Y.-S. Shim, S. H. Lee, Y. Kim, C. W. Moon, D. H. Kim, S. Y. Lee, T. Kim, H. K. Park, M. G. Lee, J.-M. Jeon, K. T. Nam, M. Kim, J. K. Kim, J. Oh, H. W. Jang, *J. Mater. Chem. A* **2016**, *4*, 9477.
[8] S. Chu, S. Vanka, Y. Wang, J. Gim, Y. Wang, Y.-H. Ra, R. Hovden, H. Guo, I. Shih, Z. Mi, *ACS Energy Lett.* **2018**, *3*, 307.
[9] S. Chen, L.-W. Wang, *Chem. Mater.* **2012**, *24*, 3659.
[10] S. E. Jun, J. K. Lee, S. Ryu, H. W. Jang, *ChemCatChem* **2023**, *15*, 202300926.
[11] T. F. Jaramillo, K. P. Jørgensen, J. Bonde, J. H. Nielsen, S. Horch, I. Chorkendorff, *Science* **2007**, *317*, 100.
[12] K. C. Kwon, S. Choi, K. Hong, C. W. Moon, Y.-S. Shim, D. H. Kim, T. Kim, W. Sohn, J.-M. Jeon, C.-H. Lee, K. T. Nam, S. Han, S. Y. Kim, H. W. Jang, *Energy Environ. Sci.* **2016**, *9*, 2240.
[13] D. Voiry, H. S. Shin, K. P. Loh, M. Chhowalla, *Nat. Rev. Chem.* **2018**, *2*, 0105.
[14] P. Gnanasekar, D. Periyanagounder, P. Varadhan, J.-H. He, J. Kulandaivel, *ACS Appl. Mater. Interfaces* **2019**, *11*, 44179.
[15] H. Li, C. Tsai, A. L. Koh, L. Cai, A. W. Contryman, A. H. Fragapane, J. Zhao, H. S. Han, H. C. Manoharan, F. Abild-Pedersen, J. K. Nørskov, X. Zheng, *Nat. Mater.* **2016**, *15*, 48.
[16] G. Li, D. Zhang, Q. Qiao, Y. Yu, D. Peterson, A. Zafar, R. Kumar, S. Curtarolo, F. Hunte, S. Shannon, Y. Zhu, W. Yang, L. Cao, *J. Am. Chem. Soc.* **2016**, *138*, 16632.
[17] J. Zhu, Z.-C. Wang, H. Dai, Q. Wang, R. Yang, H. Yu, M. Liao, J. Zhang, W. Chen, Z. Wei, N. Li, L. Du, D. Shi, W. Wang, L. Zhang, Y. Jiang, G. Zhang, *Nat. Commun.* **2019**, *10*, 1348.
[18] J. Deng, H. Li, J. Xiao, Y. Tu, D. Deng, H. Yang, H. Tian, J. Li, P. Ren, X. Bao, *Energy Environ. Sci.* **2015**, *8*, 1594.
[19] S. E. Jun, S.-P. Hong, S. Choi, C. Kim, S. G. Ji, I. J. Park, S. A. Lee, J. W. Yang, T. H. Lee, W. Sohn, J. Y. Kim, H. W. Jang, *Small* **2021**, *17*, 2103457.
[20] J. Kim, A. Park, J. Kim, S. J. Kwak, J. Y. Lee, D. Lee, S. Kim, B. K. Choi, S. Kim, J. Kwag, Y. Kim, S. Jeon, W. C. Lee, T. Hyeon, C.-H. Lee, W. B. Lee, J. Park, *Adv. Mater.* **2022**, *34*, 2206066.
[21] X. Zhang, F. Meng, S. Mao, Q. Ding, M. J. Shearer, M. S. Faber, J. Chen, R. J. Hamers, S. Jin, *Energy Environ. Sci.* **2015**, *8*, 862.
[22] S. Choi, C. Kim, J. Y. Lee, T. H. Lee, K. C. Kwon, S. Kang, S. A. Lee, K. S. Choi, J. M. Suh, K. Hong, S. E. Jun, W. K. Kim, S. H. Ahn, S. Han, S. Y. Kim, C.-H. Lee, H. W. Jang, *Chem. Eng. J.* **2021**, *418*, 129369.
[23] S. Seo, S. Kim, H. Choi, J. Lee, H. Yoon, G. Piao, J.-C. Park, Y. Jung, J. Song, S. Y. Jeong, H. Park, S. Lee, *Adv. Sci.* **2019**, *6*, 1900301.
[24] S. E. Jun, S. Choi, S. Choi, T. H. Lee, C. Kim, J. W. Yang, W.-O. Choe, I.-H. Im, C.-J. Kim, H. W. Jang, *Nano-Micro Lett.* **2021**, *13*, 81.
[25] K. Kang, S. Xie, L. Huang, Y. Han, P. Y. Huang, K. F. Mak, C.-J. Kim, D. Muller, J. Park, *Nature* **2015**, *520*, 656.
[26] A. Londoño-Calderon, R. Dhall, C. Ophus, M. Schneider, Y. Wang, E. Dervishi, H. S. Kang, C.-H. Lee, J. Yoo, M. T. Pettes, *Nano Lett.* **2022**, *22*, 2578.
[27] K. Kang, K.-H. Lee, Y. Han, H. Gao, S. Xie, D. A. Muller, J. Park, *Nature* **2017**, *550*, 229.
[28] B. E. Conway, B. V. Tilak, *Electrochim. Acta.* **2002**, *47*, 3571.
[29] J. Y. Lee, J.-H. Shin, G.-H. Lee, C.-H. Lee, *Nanomater* **2016**, *6*, 193.
[30] S. E. Jun, J. K. Lee, H. W. Jang, *Energy Adv.* **2023**, *2*, 34.
[31] J. Y. Lee, S. Kang, D. Lee, S. Choi, S. Yang, K. Kim, Y. S. Kim, K. C. Kwon, S. H. Choi, S. M. Kim, J. Kim, J. Park, H. Park, W. Huh, H. S. Kang, S. W. Lee, H.-G. Park, M. J. Ko, H. Cheng, S. Han, H. W. Jang, C.-H. Lee, *Nano Energy* **2019**, *65*, 104053.
[32] X. Zhang, Q.-H. Tan, J.-B. Wu, W. Shi, P.-H. Tan, *Nanoscale* **2016**, *8*, 6435.
[33] S. Kang, Y. S. Kim, J. H. Jeong, J. Kwon, J. H. Kim, Y. Jung, J. C. Kim, B. Kim, S. H. Bae, P. Y. Huang, J. C. Hone, H. Y. Jeong, J.-W. Park, C.-H. Lee, G.-H. Lee, *ACS Appl. Mater. Interfaces* **2021**, *13*, 1245.
[34] W. Yang, H. Kawai, M. Bosman, B. Tang, J. Chai, W. L. Tay, J. Yang, H. L. Seng, H. Zhu, H. Gong, H. Liu, K. E. J. Goh, S. Wang, D. Chi, *Nanoscale* **2018**, *10*, 22927.
[35] D. Vikraman, S. Hussain, S. A. Patil, L. Truong, A. A. Arbab, S. H. Jeong, S.-H. Chun, J. Jung, H.-S. Kim, *ACS Appl. Mater. Interfaces* **2021**, *13*, 5061.
[36] K. Chen, X. Wan, W. Xie, J. Wen, Z. Kang, X. Zeng, H. Chen, J. Xu, *Adv. Mater.* **2015**, *27*, 6431.
[37] J. Shi, R. Tong, X. Zhou, Y. Gong, Z. Zhang, Q. Ji, Y. Zhang, Q. Fang, L. Gu, X. Wang, Z. Liu, Y. Zhang, *Adv. Mater.* **2016**, *28*, 10664.
[38] M.-H. Chiu, W.-H. Tseng, H.-L. Tang, Y.-H. Chang, C.-H. Chen, W.-T. Hsu, W.-H. Chang, C.-I. Wu, L.-J. Li, *Adv. Funct. Mater.* **2017**, *27*, 1603756.
[39] F. M. Pesci, M. S. Sokolikova, C. Grotta, P. C. Sherrell, F. Reale, K. Sharda, N. Ni, P. Palczynski, C. Mattevi, *ACS Catal.* **2017**, *7*, 4990.
[40] E. S. Kadantsev, P. Hawrylak, *Solid State Commun.* **2012**, *152*, 909.
[41] C. Zhang, C. Gong, Y. Nie, K.-A. Min, C. Liang, Y. J. Oh, H. Zhang, W. Wang, S. Hong, L. Colombo, *2D Mater.* **2017**, *4*, 015026.
[42] R. Chen, L. Meng, W. Xu, L. Li, *Small* **2023**, *20*, 2304807.
[43] P. Kuang, L. Zhang, B. Cheng, J. Yu, *Appl. Catal., B.* **2017**, *218*, 570.

